Role of doping and defect quenching in antiferroelectric $NaNbO_3$ from first principles

Lorenzo Villa* and Karsten Albe

Fachgebiet Materialmodellierung, Institut für Materialwissenschaft, TU Darmstadt, Otto-Berndt-Straße 3, D-64287 Darmstadt, Germany

(Received 4 August 2022; accepted 21 September 2022; published 5 October 2022)

The antiferroelectric $NaNbO_3$ is a candidate material for application in high-energy density dielectric capacitors. Various doping strategies have been used for installing the desired narrow double *P-E* loop behavior in this lead-free material. However, to unravel the influence of doping on the double *P-E* loops, we first need to understand the influence of doping on the defect equilibrium. In this study, we therefore calculate the formation energies, charge transition levels, and doping behavior of single defects and defect complexes in orthorhombic $NaNbO_3$ doped with Ca, Sn, and Sr by means of density functional theory (DFT). The results show that substitutions with dopants have formation energies as low as Na and O vacancies. Additionally, all defect complexes show negative binding energy, which means they are stable and very likely to form. Lastly, we show how defect quenching influences the Fermi level, which reveals how the synthesis conditions can tailor the final defect distribution.

DOI: 10.1103/PhysRevB.106.134101

I. INTRODUCTION

Extended research, aimed at improving the properties of dielectric capacitors for energy storage applications has fostered the interest in antiferroelectric (AFE) materials. AFE materials are characterized by antiparallel adjacent dipoles within the crystal structure, in contrast to ferroelectrics (FE), which leads to a zero macroscopic spontaneous polarization. However, an electric field can provide a driving force for the dipoles to become parallel, thus reaching a FE state. If this phase transition is reversible, removing the field will restore the system to an AFE state with zero remnant polarization. Thus, its hysteresis behavior displays a double *P-E* loop, resulting in both, high energy density and efficiency [1]. In this class of materials, sodium niobate (with chemical formula $NaNbO_3$) is amongst the most promising alternatives [1,2] to the toxic lead-containing compounds, such as $PbZrO_3$-based ceramics [3]. $NaNbO_3$ is a perovskite compound, which exhibits many phase transitions characterized by a combination of tilted oxygen octahedra and off-centered displacements of Nb^5+ ions in the lattice [4–6]. The sequence of the phase transitions with relative nomenclature is as the following: rhombohedral *N* (*R3c*, below 173K), orthorhombic *P* (*Pbcm*, 173 to 633 K), orthorhombic *R* (*Pmnm* 633 to 753 K), orthorhombic *S* (*Pnmm*, 753 to 793 K), orthorhombic T_1 (*Cmcm*, 793 to 848 K), tetragonal T_2 (*P4/mbm*, 848 to 913 K), cubic *C* ($Pm\bar{3}m$, above 913 K) [2,4,6,7]. At room temperature, the AFE *P* phase might coexist with a FE polymorph named *Q* phase (space group $Pmc2_1$). These two polymorphs are relatively close in energy and the phase transition from the *P* to the *Q* phase occurs by applying a sufficient external field or through chemical modification of the compound [6,8].

In $NaNbO_3$, the double *P-E* hysteresis loops are rarely observed, since the phase transition is not completely reversible because the field-induced FE *Q* phase remains in a metastable state. As a consequence, the system preserves a spontaneous polarization even without applied field [9,10]. For energy storage applications, however, materials displaying a narrow double *P-E* loop are of interest. In order to reach this condition, the AFE phase needs to be stabilized over the FE phase, so that the AFE-FE phase transition is reversible and the system does not show spontaneous polarization [8]. The most common approach in this direction is chemical modification of the compound by doping [1]. In recent years, different dopants have been investigated [11]. Gao *et al* reported double *P-E* loops in the $(BiScO_3)_x$-$(NaNbO_3)_{1-x}$ solid solutions [12]. More specifically, they showed that doping $NaNbO_3$ with Bi^3+ and Sc^3+ stabilizes the AFE phase without changing the crystal symmetry of $NaNbO_3$. Other works proposed various codoping approaches, such as (Sr^2+, Zr^4+) [13], (Ca^2+, Hf^4+) [14], (Sr^2+, Hf^4+) [15], and (Ca^2+, Sr^4+) [16]. Zhang *et al.* [8] have found that the energy efficiency of $NaNbO_3$ can be significantly improved upon the addition of $SrSnO_3$. When impurities are introduced into the system, they will interact with the present intrinsic defects, forming defect dipoles for example. This has an impact on the role that dopants play in the stabilization of the AFE phase. It has been proposed [17,18] that the presence of defect dipoles plays a crucial role in improving the AFE double *P-E* loops by introducing a restoring force, which facilitates reversible domain mobility. Tan *et al* have suggested for $NaNbO_3$-based systems that dopants and intrinsic defects form defect dipoles, which affect the phase transitions and improve the AFE loops [19]. Thus, developing doping strategies for improving the AFE properties of $NaNbO_3$, requires a thorough understanding of the underlying defect mechanisms. In 2004, Shigemi and Wada [20] calculated formation energies of vacancies in $NaNbO_3$ by solely considering their neutral charge state.

*villa@mm.tu-darmstadt.de

Therefore, in our previous study, we have computed the formation energies of the vacancies and a V_{Na}-V_O-V_{Na} vacancy complex in the high-temperature cubic phase, considering all possible charge states, and we have found that Na and O vacancies are present in large concentrations in charge states -1 and $+2$, respectively [21]. Moreover, we have learned that the vacancy complex has a negative binding energy across most of the band gap, indicating its stability and its presence in large concentrations, which can affect the *P-E* loops, whereas previously only dopant-vacancy complexes were proposed as an influencing factor [19]. However, a deep investigation on the interaction between intrinsic and extrinsic defects, defect complexes and their influence on defect equilibria has, to our knowledge, not been conducted yet. Therefore, we have expanded the research in this direction.

In this work, we have studied defect formation energies in orthorhombic $NaNbO_3$ doped with (Ca,Sn) and (Sr,Sn), with additional focus for the latter on thermodynamics and electronic properties, with the goal to understand the contribution of defects to the improved *P-E* loops achieved by Zhang *et al.* [8]. In particular, we have computed the formation energies of Na,Nb and O vacancies, substitutional defects with Ca/Sr on the Na site and Sn on the Nb site, neutral and charged defect complexes. Additionally, we have computed the electron chemical potential by solving self-consistently the charge neutrality condition. For these systems, the contribution of kinetics during the cooling process from the synthesis temperature down to room temperature can be decisive for the final defect equilibrium. This problem has not been investigated yet for $NaNbO_3$. Therefore we have extended the approach employed by Shousha *et al.* [22] and Lee *et al.* [23] to extrinsic defects and defect complexes, which allows to solve the charge neutrality condition while accounting for defect quenching and fixed dopant concentrations, without neglecting the dependency of their charge state on electron chemical potential and temperature. Lastly, in order to be closer to the experimental world, we have calculated the dependency of defect concentrations and electron chemical potential on the oxygen partial pressure.

The paper is organized as follows. Section II describes the applied methodology of our calculations, Sec. III focuses on the presence of intrinsic and extrinsic defects and gives an overview of their formation energies, charge transition levels and their doping behavior in different oxygen partial pressure and quenching conditions, Sec. IV summarizes the results of the present work and draws conclusions.

II. METHODS

A. Computational details

All calculations were performed based on density functional theory (DFT) using the Vienna *ab initio* simulation package (VASP) [24–27]. The electronic wave functions were described using the projector augmented-wave method [28,29], which includes both valence and core states. To study pure $NaNbO_3$, the exchange-correlation effects were treated using the Perdew-Burke-Ernzerhof [30] formalism of the generalized-gradient approximation (GGA). All defect calculations were performed for the room-temperature stable orthorhombic phase of $NaNbO_3$ (*Pbcm*, space group No. 47) using a $2 \times 2 \times 1$ supercell, containing 160 atoms. The plane wave basis set was expanded up to a 550 eV cutoff energy. The Brillouin zone integration was performed using a Γ-centered $4 \times 4 \times 2$ k mesh for unit-cell calculations and a $2 \times 2 \times 2$ k mesh for supercell calculations. The atomic positions were relaxed until the Hellmann-Feynman forces on each atom were below 0.05 eV/Å. [31,32]. The density of states (DOS) was calculated using a Γ-centered $12 \times 12 \times 6$ k mesh. In order to obtain the saddle points necessary for the calculation of diffusion barriers, we applied the climbing image nudged elastic band method [33,34], which imposes a minimal number of constraints on the transition path. Only jumps between nearest-neighbor sites were considered.

B. Defect thermodynamics

The formation energy ΔE_D^F of a defect D in charge state q is given by [35–37]

$$\Delta E_D^F = E_D - E_P + q(E_{\mathrm{VBM}} + \mu_e) + E_{\mathrm{corr}} - \sum_i \Delta n_i \mu_i, \tag{1}$$

where q denotes the defect charge state, E_D is the total energy of the defective system, and E_P is the total energy of the perfect reference cell. The third term describes the dependence of formation energy on the (μ_e), where E_{VBM} is the position of the valence-band maximum (VBM) of the pure supercell that defines the reference energy for μ_e. E_{corr} is the correction to the unphysical electrostatic interactions between defects replica, due to the finite size of the supercell. The correction method used in this work was proposed by Kumagai *et al.* [38] The variation of the formation energy with the chemical potentials of the constituent elements is given by the last term. The difference between the number of atoms of type i in the defective cell with respect to the reference cell is denoted by Δn_i. The chemical potential μ_i of constituent i can be rewritten as

$$\mu_i = \mu_i^{\mathrm{ref}} + \Delta\mu_i, \tag{2}$$

where μ_i^{ref} denotes the chemical potential of the constituent element in its stable elemental phase. The chemical potentials were calculated from the data reported in the Materials Project database [39,40], whose set of parameters is consistent with the ones we have used in this work. The phase stability diagram was constructed for the orthorhombic phase of $NaNbO_3$, using the python materials genomics (PYMATGEN) library [41,42].

A thermodynamic transition level refers to the electron chemical potential at which the formation energy of a given defect becomes equal at charge states q_1 and q_2 and is given by

$$\epsilon = -\frac{\Delta E_D^F(q_1) - \Delta E_D^F(q_2)}{q_1 - q_2}, \tag{3}$$

where $\Delta E_D^F(q_1)$ and $\Delta E_D^F(q_2)$ denote respectively the formation energy of the defect in charge states q_1 and q_2, when μ_e is at the VBM. Under thermodynamic equilibrium conditions, the concentration of a defect D in charge state q can be

calculated by

$$[D_q] = N_{\text{sites}} \exp\left(-\frac{\Delta E^F_{q,D}(\mu_e)}{k_B T}\right), \tag{4}$$

where q is the charge, N_{sites} is the concentration of the corresponding lattice sites, and k_B is the Boltzmann constant.

Note that the electron chemical potential (μ_e) in Eq. (1) is not a free parameter and can be calculated using the charge neutrality condition,

$$n_e + n_A = n_h + n_D, \tag{5}$$

where n_e and n_h are respectively the electron and holes carrier concentrations, and n_D and n_A are respectively the concentrations of donors and acceptors. Given different defect species (D) in different charge states (q), Eq. (5) can be expressed as

$$\sum_{q,D} q \cdot [D_q] - n_e + n_h = 0. \tag{6}$$

Intrinsic carrier concentrations are derived by integrating the number of unoccupied states up to the VBM (E_{VBM}) for holes,

$$n_h = \int_{-\infty}^{E_{\text{VBM}}} D(\epsilon)[1 - f(\epsilon)]d\epsilon, \tag{7}$$

and the number of occupied states from the conduction-band minimum (CBM) (E_{CBM}) for electrons,

$$n_e = \int_{E_{\text{CBM}}}^{+\infty} D(\epsilon) f(\epsilon) d\epsilon, \tag{8}$$

where $f(\epsilon, \mu_e) = [\exp(\epsilon - \mu_e)/k_B T)]^{-1}$ is the Fermi-Dirac distribution.

In this work, the two integrals were computed as a Riemann sum over the energies in the calculated density of states, as adopted by PYMATGEN [41]. The equilibrium electron chemical potential μ_e was then determined self-consistently by solving the charge neutrality condition at fixed temperature with μ_e as a variable.

C. Oxygen chemical potential

Defect formation energies depend on the chemical potential (μ_e and μ_i) of the reservoir, which in the case of oxygen is directly linked to the partial pressure. Using the ideal gas law, it is possible to relate the oxygen chemical potential with temperature and partial pressure, according to [43,44]

$$\mu_{\text{O}}(T, p_{\text{O}_2}) = \mu_{\text{O}}(T, p^0) + \frac{1}{2} k_B T \ln\left(\frac{p_{\text{O}_2}}{p^0}\right), \tag{9}$$

where k_B is the Boltzmann constant, T the temperature, p^0 the reference pressure, and p_{O_2} the oxygen partial pressure. We have chosen the computed energy of the O_2 molecule at the 0-K reference state $\mu_{\text{O}}(0K, p^0)$, and the temperature dependence $\mu_{\text{O}}(T, p^0)$ has been determined using thermochemical tables [45], following Ref. [43]. With this definition it is possible to obtain the oxygen chemical potential starting from its partial pressure in the experimental conditions, or alternatively to evaluate the defect concentrations and the electron chemical potential as a function of the oxygen partial pressure, which is useful to compare the results with experimental data.

D. Defect quenching

The synthesis of materials often relies on quickly cooling down the sample, in order to preserve its high temperature state down at room temperature. This requires that quenching is accounted for in a theoretical and computational model which studies defect thermodynamics. A first possible approach to tackle the problem is to compute μ_e at high temperature, compute the defect charges in the high temperature equilibrium and fix them at low temperature, as proposed by Canepa *et al.* [46]. The problem with this approach is that the charge states of the defects are assumed to be constant. Since charge carriers have enough mobility to diffuse and equilibrate when temperature is decreased, shifting μ_e due to a temperature change and/or a phase transformation can affect the charges the defects can assume. Hence, even if their concentration is fixed, their contribution to the charge neutrality can be completely different from one condition to the other.

We encounter a similar problem when extrinsic defects are included in a defect thermodynamics study. In the experimental world, when chemical doping/substitution is performed, the concentration of extrinsic defects inside the sample is going to be fixed from the synthesis stage. The common approach, in this context, is to guess the charge state of the doped system, by setting up chemical reactions derived from the most common oxidation states of the substituting element. Subsequently, its contribution to the charge neutrality condition is added as $q \cdot [D_{\text{fix}}]$, where q is the charge of the extrinsic defect and $[D_{\text{fix}}]$ is the fixed concentration [44]. Also in this case, the charge state dependency on temperature (T) and μ_e of the extrinsic defect has been completely neglected. While generally the oxidation states can be a proper descriptor, we might also encounter a situation where the dopant's charge behaves in an unexpected way, or simply the assumed charge is not the most stable one for all T and μ_e values.

In this work we have employed the following novel scheme to solve both of these problems, namely to allow to fix defect concentrations (both intrinsic and extrinsic) without neglecting the dependency of the charge states on phase, temperature and electron chemical potential. We start from the approach employed by Shousha *et al.* [22] and Lee *et al.*, and we show how this model can be extended to account for extrinsic defects and defect complexes as well, without introducing additional *a priori* assumptions.

As already introduced in Sec. II B, the total charge associated with a generic defect specie D is given by

$$Q_D = \sum_q q \cdot [D_q], \tag{10}$$

where q is the charge state and $[D_q]$ is the concentration of defect D in charge state q. We introduce the quantity $[el]$, which is the total concentration of element el (or a vacancy of the element) across all defect species. Therefore it is the sum of the concentrations of defect species d which contain el, in all of their possible charge states q:

$$[el] = \sum_{d,q} [d_q] = \sum_{d,q} N_d e^{-\beta E_{d,q}}, \tag{11}$$

where β is equal to $1/k_BT$ and $E_{d,q}$ is the formation energy of defect d in charge state q, as defined in Sec. II B (the symbol "Δ" has been removed to lighten the notation). If we divide and multiply $[D_q]$ by $[el]$ we can explicate the term:

$$w_{D,q}(\mu_e, T) = \frac{[D_q]}{[el]} = \frac{N_D e^{-\beta E_{D,q}}}{\sum_{d,q} N_d e^{-\beta E_{d,q}}}, \tag{12}$$

which depends on temperature and μ_e and represents the weight of the concentration of defect D in charge state q with respect to the total concentration of the element. Having rewritten $[D_q]$ as $w_{D,q}(\mu, T)\,[el]$, it is possible now to assume that, in "fixed" conditions, the total concentration of the element el is equal to the target value of $[el^{\text{fix}}]$, which in practice might be a high-temperature concentration value arising from quenching, or the fixed concentration of a dopant. In this way, it is possible to compute the concentration of defect D in charge state q in "fixed" conditions, without neglecting its temperature and μ_e dependence and/or performing further assumptions:

$$\left[D_q^{\text{fix}}\right] = w_{D,q}(\mu, T)\,[el^{\text{fix}}] = [D_q] \cdot \frac{[el^{\text{fix}}]}{[el]}. \tag{13}$$

By doing so we rely on the behavior that the defect would show if it was allowed to equilibrate with its reservoir, but we constrain its concentration to a target value.

The same approach can be extended to describe defect complexes. The complex is treated as an independent defect specie. Like in Eq. (10), the charge associated to complex C in charge q is given by

$$Q_C = \sum_q q \cdot [C_q] \tag{14}$$

and its concentration in equilibrium conditions, following Eq. (4), is given by $N_C e^{-\beta E_{C,q}}$, where $E_{C,q}$ is the formation energy and N_C is the site multiplicity of the complex. It is possible to write $[C_q]$ in terms of the formation energy of the single defects (E_D) that constitute the complex and its binding energy, which is defined as

$$E_b = E_C - \sum_D E_D. \tag{15}$$

We obtain

$$[C_q] = N_C\, e^{-\beta E_b} \prod_D e^{-\beta E_{D,q}} = N_C\, e^{-\beta E_b} \prod_D \frac{[D_q]}{N_D}. \tag{16}$$

Following the same approach used for single defects in Eq. (12), we can rewrite $[C_q]$ as

$$[C_q] = N_C\, e^{-\beta E_b} \prod_D [el] \frac{w_{D,q}}{N_D}. \tag{17}$$

Out of the species from which the complex is made, we define the subset of defects whose concentrations need to be fixed (named D^f). In this way, we can perform the same assumption as in the case of single defects, namely, we substitute $[el]$ with $[el^{\text{fix}}]$ for the species belonging to the subset D^f, while nothing changes for the remaining subset of species which are allowed to equilibrate with the reservoir (D^e). We obtain

$$\left[C_q^{\text{fix}}\right] = N_C e^{-\beta E_b} \prod_{D\in D^e} [el] \frac{w_{D,q}}{N_D} \prod_{D\in D^f} [el^{\text{fix}}] \frac{w_{D,q}}{N_D}. \tag{18}$$

Comparing Eqs. (17) and (18), we can rewrite $[C_q^{\text{fix}}]$ as

$$\left[C_q^{\text{fix}}\right] = [C_q] \cdot \prod_{D\in D^f} \frac{[el^{\text{fix}}]}{[el]} = N_C e^{-\beta E_{C,q}} \cdot \prod_{D\in D^f} \frac{[el^{\text{fix}}]}{[el]}. \tag{19}$$

By expressing $[C_q^{\text{fix}}]$ as in Eq. (19), we leave the expression for the concentration of the complex unchanged, still depending on its formation energy and without relying explicitly on the binding energy. Simply, it is enough to correct the equilibrium value with the factor $[el^{\text{fix}}]/[el]$ for the species with fixed concentration, in a similar fashion to Eq. (13).

Figure 1 summarises all the different conditions this model can explore. The schematic lattice in the top figure represents the starting conditions, which in the case of quenching is usually a phase stable at high temperature (phase β at temperature T_β). Once the defect distribution in this system has been computed, it can be used to evaluate how a different phase (α) at a lower temperature (T_α) reacts when all defects or a subset of defects are frozen in from the high temperature phase. In fact, following Eqs. (13) and (19), it is possible to quench only a subset of defects, while letting the rest equilibrate. This can be particularly useful in case some defects are particularly

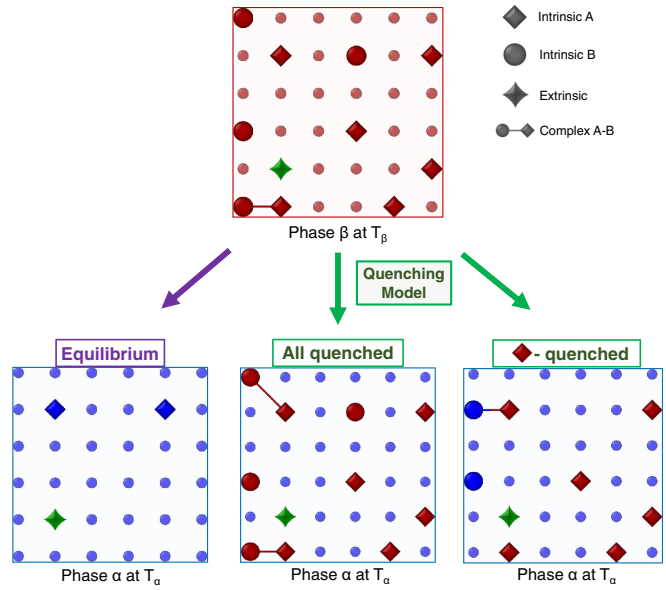

FIG. 1. Schematic representation of the different conditions our quenching model can explore. A defect distribution equilibrated in an initial phase β at temperature T_β can be quenched in a different phase α at temperature T_α. Quenching can involve all defect species or just a subset, letting the rest equilibrate in the target conditions. The charge states of the quenched defects still depend on temperature and electron chemical potential in the target phase. Defect complexes depend on the concentrations of single defects but are still allowed to associate and dissociate, with probability depending on their binding energy in the target phase. The concentrations of extrinsic defects are fixed to the experimental values, but their charge states still depend on temperature and electron chemical potential in the target phase as for intrinsic defects.

TABLE I. Values of lattice constants a, b, c (Å) and energy gap E_g (eV) of orthorhombic $NaNbO_3$ (space group *Pbcm*, No. 57), computed with the PBE [30] exchange-correlation functional and confronted with computational data by Shigemi and Wada [20], the Materials Project database [39,40] and experimental data.

	a (Å)	b (Å)	c (Å)	E_g (eV)
PBE	5.569	5.677	15.571	2.48
Ref PBE [20]	5.560	5.629	15.552	2.34
MP Database (PBE) [39,40]	5.598	5.687	15.681	2.36
Exp	5.532 [6]	5.563 [6]	15.645 [6]	3.42 [47]

mobile, and therefore the original defect distribution is not preserved during the cooling process. Moreover, even if the concentrations of single defects are fixed, defect complexes can still form and dissolve, and the association probability is dependent implicitly on the binding energy, as computed in the target phase (phase α at temperature T_α). Lastly, the concentration of extrinsic defects is hold constant to the experimental value in all conditions.

In this work, we have studied the variation of μ_e in orthorhombic $NaNbO_3$ with different quenching conditions, with initial temperature set to the sintering temperature of 1633 K [8] and final temperature set to 300 K (RT).

III. RESULTS AND DISCUSSIONS

A. Electronic structure

The study of defect thermodynamics requires preliminary calculations. In particular, the relaxed bulk structure and the electronic structure need to be determined. In fact, the total energy of the bulk supercell and the VBM are required for the evaluation of defect formation energies [Eq. (1)], while the density of states (DOS) is used in the computation of electrons and holes concentrations [Eqs. (7) and (8)]. The computed values of lattice parameters and energy gap are reported and compared with literature in Table I. The band structure and DOS are reported in Fig. 2.

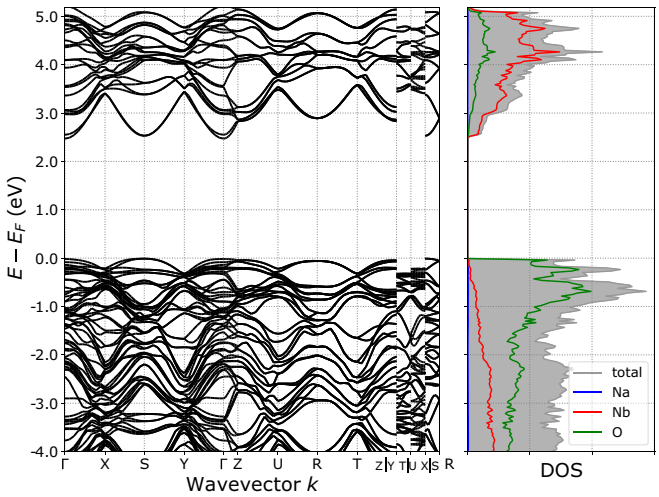

FIG. 2. Band structure and density of states of orthorhombic $NaNbO_3$ (space group *Pbcm*).

TABLE II. Formation energy per atom for all the compounds used to compute the stability diagram.

Composition	Structure	Formation energy p.a (eV)
$Nb_{12}O_{29}$	Orthorhombic (*Cmcm*)	−3.05
NaO_2	Orthorhombic (*Pnnm*)	−0.91
Nb_2O_5	Monoclinic (*P*2)	−3.05
Na_2O_2	Hexagonal ($P\bar{6}2m$)	−1.31
$NaNb_{10}O_{18}$	Monoclinic ($P2_1/c$)	−2.79
Na_2O	Cubic ($Fm\bar{3}m$)	−1.45
Nb	Cubic ($Im\bar{3}m$)	0
NbO_2	Tetragonal ($I4_1/a$)	−2.91
$NaNb_{13}O_{33}$	Triclinic (*P*1)	−3.03
$NaNb_3O_8$	Orthorhombic (*Pmmn*)	−2.97
Na	Hexagonal ($P6_3/mmc$)	0
$Na_2Nb_3O_6$	Trigonal ($P\bar{3}1c$)	−2.67
O_2	Monoclinic ($C2/m$)	0
$NaNbO_2$	Hexagonal ($P6_3/mmc$)	−2.54
Na_5NbO_5	Monoclinic ($C2/c$)	−2.25
NbO	Cubic ($Pm\bar{3}m$)	−2.29
$NaNbO_3$	Orthorhombic (*Pbcm*)	−2.83
Na_3NbO_4	Monoclinic ($C2/m$)	−2.52

The edge of the valence band is mainly given by O *p* states, while the edge of the conduction band is mainly composed of Nb *d* states. The VBM is in the S point, with the Γ point being very close in energy, and the CBM is in the Γ point, yielding an indirect gap of 2.48 eV. It is well known that the semilocal nature of the PBE functional tends to underestimate the band gap. However, it does not constitute a problem for defect equilibrium calculations, because the biggest contributions to the carrier concentrations are given by the curvature of the bands near the band edges, and by the relative distance of the thermodynamic charge transition levels to the band edges.

B. Stability diagram

The next step in the calculation of defect properties is to define the thermodynamic reservoirs. This requires the calculation of the semigrandcanonical phase diagram, which shows the stability areas as function of the chemical potentials of the constituents. The list of the stable phases with relative formation energies is reported in Table II. The DFT data used to generate the phase diagram was obtained from the Materials Project database (version 2020_09_08) [48]. The parameters used to compute the database are consistent with the ones used in our calculations.

The stability diagram, calculated from the formation energies of each competing phase, is shown in Fig. 3. The chemical potential range of the constituents is restricted by the condition that its sum must be equal to the formation enthalpy of $NaNbO_3$:

$$\Delta\mu_{\mathrm{Na}} + \Delta\mu_{\mathrm{Nb}} + 3\Delta\mu_{\mathrm{O}} = \Delta H_f[\mathrm{NaNbO_3}]. \quad (20)$$

For fixed values of $\Delta\mu_{\mathrm{Na}} + \Delta\mu_{\mathrm{Nb}}$, the value of $\Delta\mu_{\mathrm{O}}$ is determined by this condition. The stability range of $NaNbO_3$ is further limited by the presence of competing phases, and is represented by the area delimited by points A to D in Fig. 3. More specifically, given a generic competing phase of composition $Na_iNb_jO_k$, the chemical potentials have to

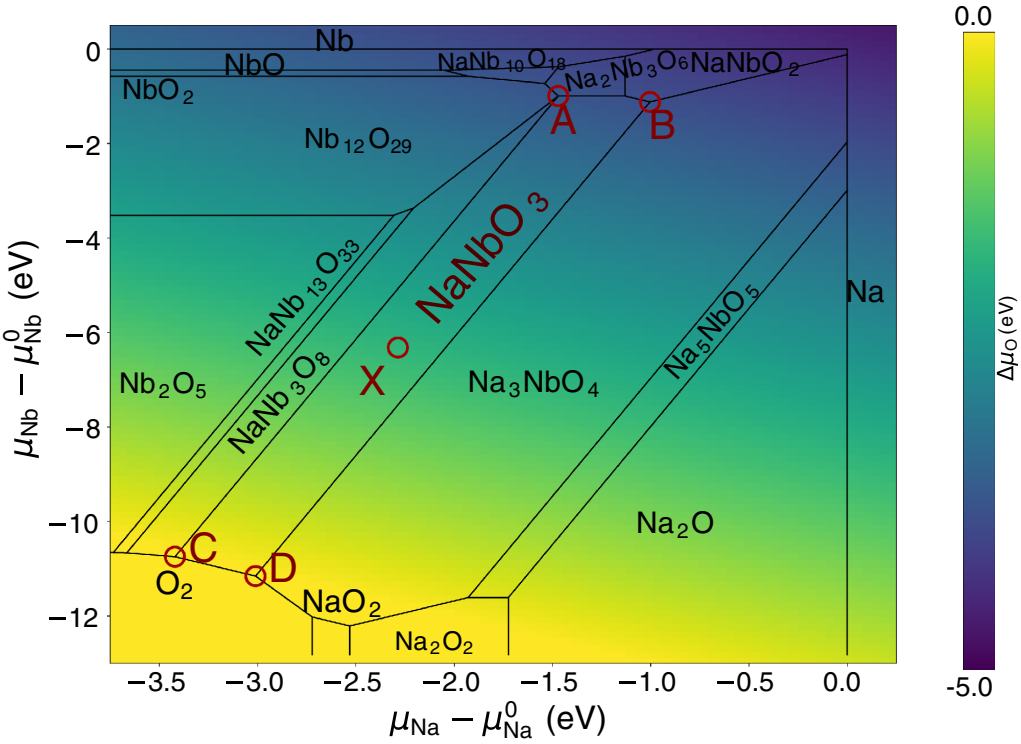

FIG. 3. Stability diagram of the ternary Na-Nb-O system, as derived from the data in Table II. The defect formation energies are discussed in terms of the chemical potentials at the points from A to D and point X, as reported in Table III.

satisfy the condition:

$$i\Delta\mu_{\mathrm{Na}} + j\Delta\mu_{\mathrm{Nb}} + k\Delta\mu_{\mathrm{O}} \leqslant \Delta H_f[\mathrm{Na}_i\mathrm{Nb}_j\mathrm{O}_k]. \qquad (21)$$

The defect formation energies were computed for different thermodynamic reservoirs, represented in the figure by the labels from A to D and X. Regions from A to D are generic limits of stability, which space from O-rich conditions (point C) to Na-rich and Nb-rich conditions (point A). It is also of interest to evaluate the formation energies using a thermodynamic reservoir that represent the experimental conditions. In particular, we fix the oxygen chemical potential ($\Delta\mu_{\mathrm{O}}$) to its value at the conditions of temperature and partial pressure of the sintering process, according to the work of Zhang *et al.* [8] ($T = 1633$ K and $p_{\mathrm{O}_2} = 0.2$ atm). For details on the calculation of this quantity we refer to Eq. (9), described in Sec. II C. With this procedure we obtain $\Delta\mu_{\mathrm{O}} = -1.92$ eV, which is indicated by the point X in Fig. 3. In order to obtain the chemical potential of the extrinsic elements (Ca, Sr, and Sn), we have generated the stability diagrams for $CaSnO_3$ and $SrSnO_3$ in the same fashion as for $NaNbO_3$. The reference elemental phases of Sr, Ca, and Sn are trigonal ($R\bar{3}m$), hexagonal ($P6_3/mmc$), and cubic ($Fd\bar{3}m$), respectively. Since the range of stability varies for every compound, we have evaluated the chemical potential of the elements in O-poor and O-rich regions, assigning the former to reservoirs A and B and the latter to reservoirs C and D. In region X, the values are taken from the center of the stability region, having fixed $\Delta\mu_{\mathrm{O}}$ to -1.92 eV. This procedure is carried out mainly to be able to compare the formation energies of the extrinsic defects with the intrinsic ones. However, when we solve the charge neutrality, extrinsic defects in $NaNbO_3$ are not free to exchange particles with a reservoir, as their concentrations are fixed to the experimental values. The chemical potential values associated to the labeled regions in the stability diagram are reported in Table III.

TABLE III. Values of the chemical potentials of the individual elements for each of the labeled regions in the stability diagram (Fig. 3).

Reservoir	$\Delta\mu_{\mathrm{O}}$	$\Delta\mu_{\mathrm{Nb}}$	$\Delta\mu_{\mathrm{Na}}$	$\Delta\mu_{\mathrm{Sr}}$	$\Delta\mu_{\mathrm{Ca}}$	$\Delta\mu_{\mathrm{Sn}}$
A	−3.94	−0.90	−1.49	−3.50	−4	0
B	−4.06	−1.08	−0.96	−3.50	−4	0
C	0	−10.72	−3.49	−6.50	−7	−6
D	0	−11.22	−2.99	−6.50	−7	−6
X	−1.92	−6.15	−2.26	−5.79	−5.92	−4.19

C. Defect formation energies

In this study, we have computed defect formation energies according to Eq. (1), in the different regions of the stability diagram reported in Fig. 3 and Table III. Because of the finite size of the supercell, we have corrected the unphysical electrostatic interactions between charged defect replicas, using the method proposed by Kumagai *et al.* [38]. For each defect, we have computed all possible charge states, in order to obtain the charge transition levels [Eq. (3)], and to properly describe the contribution of each defect specie to the charge neutrality condition. As far as intrinsic defects are concerned, we have studied the formation energies of Na, Nb, and O vacancies and the complex formed by a sodium and an oxygen vacancy

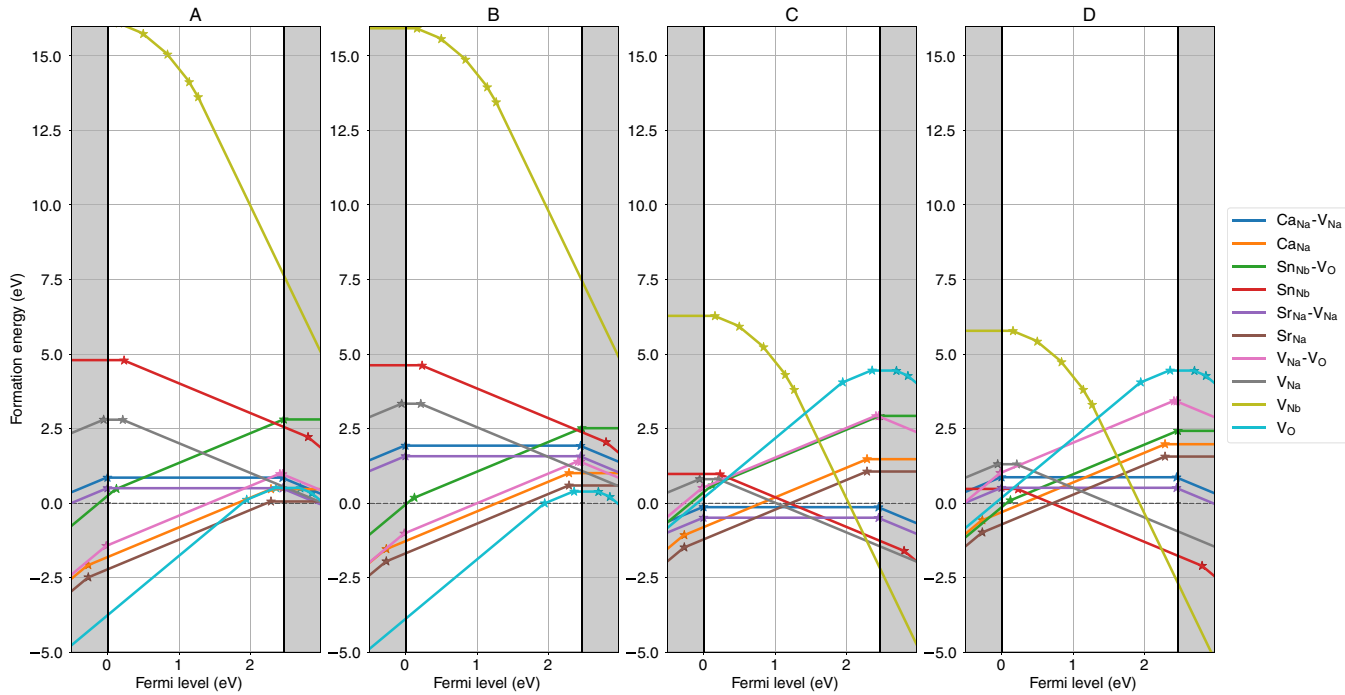

FIG. 4. Defect formation energies as a function of the Fermi level position for representative thermodynamic conditions (shown in Fig. 3). The stars on the formation energy curves represent charge transitions.

(V_{Na}-V_O). Regarding extrinsic defects, we have evaluated the substitution on the Na-site with Sr and Ca (Sr_{Na}, Ca_{Na}) and on the Nb site with Sn (Sn_{Nb}). Additionally, we have computed the formation energies of defect complexes. In particular, the complexes formed by the substitution on the Na site with a neighboring Na vacancy (Sr_{Na}-V_{Na} and Ca_{Na}-V_{Na}) and by Sn on the Nb site with a neighboring O vacancy (Sn_{Nb}-V_O). In order to limit, the number of possible combinations, and therefore the number of required DFT calculations, we have restricted out study to complexes formed by a maximum of two point defects. However, we do not exclude the possibility of complexes formed by three point defects, as we have found previously [21] that the complex V_{Na}-V_O-V_{Na} is likely present in cubic $NaNbO_3$.

The formation energies computed in the boundary regions of the stability diagram are plotted as a function of the Fermi level in Fig. 4. The stars in the plot represent the charge transition levels, which are plotted separately in Fig. 5. As far as intrinsic defects are concerned, Na vacancies are acceptors as expected, being stable in charge state of -1 across almost all the band gap. O vacancies are mostly donors in charge state $+2$, however they display a deep transition level from $+2$ to $+1$ at 0.5 eV below the CBM, with a shallower transition from $+1$ to 0 (0.1 eV below the CBM). Nb vacancies presents more scattered transitions across the gap, with -5 being the most stable from approximately mid-gap to the CBM. The stable charges of extrinsic defects also follow the behavior of their common oxidation states. In fact both Sr_{Na} and Ca_{Na} are both donors with $+1$ charge state. They both present a $+1/0$ transition at 0.2 eV below CBM. Sn_{Nb} is an acceptor, with a $0/-1$ transition at 0.2 eV above the VBM. Regarding the defect complexes, Sr_{Na}-V_{Na} and Ca_{Na}-V_{Na} are neutral, while Sn_{Nb}-V_O and V_{Na}-V_O are both donors in $+1$ charge state. In all reservoirs, we notice that defects involving Sr have lower formation energies than Ca, both for single substitutions and complexes. In oxygen-poor conditions (A and B), intrinsic defects are dominated by oxygen vacancies. The formation energy is low also for the V_{Na}-V_O complex, indicating its presence in large concentrations. Nb vacancies show considerably high formation energies, which implies a negligible contribution in these conditions. The substitution involving the Na-site presents low formation energies, especially Sr_{Na}. Oxygen-rich conditions present a different situation, with Na

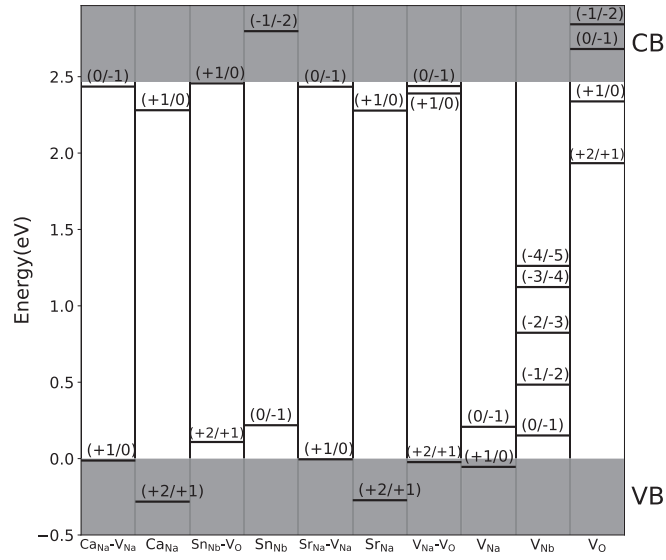

FIG. 5. Charge transition levels. The energy levels in the valence band (VB) and conduction band (CB) are indicated by the grey shaded areas.

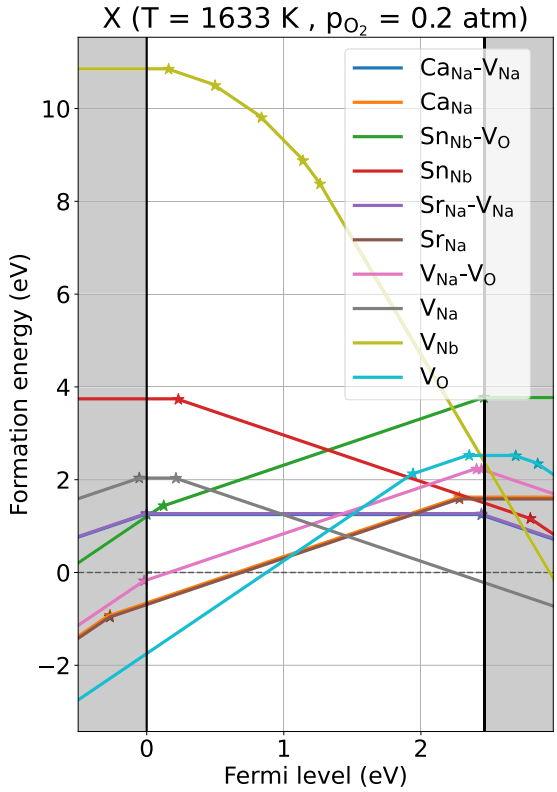

FIG. 6. Defect formation energies as a function of the Fermi level position for thermodynamic conditions representative of the experimental conditions (reported in Table III). The stars on the formation energy curves represent charge transitions.

vacancies dominating the intrinsic defects, and Nb vacancies which show considerably lower formation energies with respect to O-poor conditions. This is due to the large range of $\Delta\mu_{Nb}$ between the extrema of the stability diagram (more than 10 eV). The balance shifts also for extrinsic defects, with Sn_{Nb} having mostly the lowest formation energies. In these points of the phase diagram, some of the defects can display formation energies which are particularly small (Sr_{Na} in point A) or even negative (Sr_{Na}-V_{Na} and Ca_{Na}-V_{Na} in point C). This is due to the fact that the reservoirs used for the calculations are at the boundary of stability of $NaNbO_3$. Computing the formation energies in these regions is useful to present a complete picture at the edges of stability of $NaNbO_3$. However, they are only hypothetical conditions and do not represent the experimental conditions during the synthesis of the material. To bridge this gap, we have computed the formation energies for temperature and pressure conditions that are present during sintering of $NaNbO_3$ (X point in Table III). Figure 6 shows the result. We notice that none of the defects present extremely low formation energies, which is in line with our expectation, since we are mimicking the real conditions. However, it is interesting how the formation energies of V_{Na}, V_O and V_{Na}-V_O are still relatively low, which confirms their stability and that they will have an important contribution on charge neutrality. Moreover, extrinsic defects display energies within the same range, indicating their stability during the synthesis process. This explains how it is possible to push the doping with $SrSnO_3$ to large concentration values (up to 5% wt.) [8].

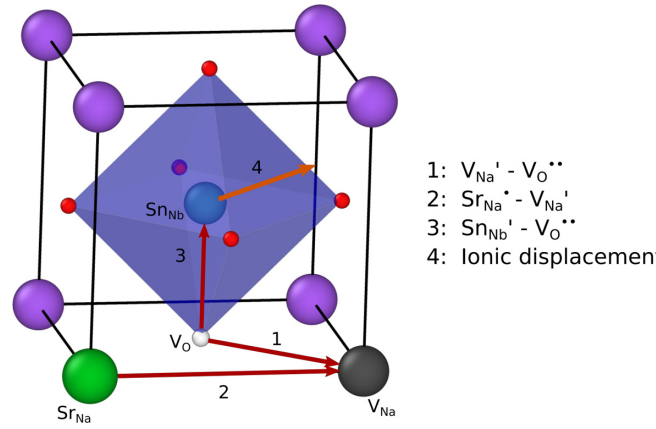

FIG. 7. Configurations of the defect dipoles in the pseudo-cubic unit cell of $NaNbO_3$. The directions are compared with the ionic displacement in the center of the oxygen octahedron in the orthorhombic phase ($[110]_{PC}$).

D. Defect complexes

As already mentioned in Sec. III C, we have studied different defect complexes. Because the defects are charged, when they associate defect dipoles are formed. For simplicity, we show the configurations in the pseudo-cubic structure of $NaNbO_3$ in Fig. 7. The arrows represent the directions of the defect dipoles as well as the ionic displacement of the B site (Nb and Sn_{Nb}) along the [110] pseudo-cubic direction [1,49].

The key quantity to understand the stability of defect complexes is the binding energy (E_b), which is defined as the difference between the formation energy of the complex and the formation energy of single defects, as in Eq. (15). It is therefore independent of the chemical potentials. It indicates the energy cost or gain that is correlated to the defects association. We show the binding energy as a function of the Fermi level for the four computed defect complexes in Fig. 8. The change in slope are associated with the charge transitions of the different defect species. In particular, it can be seen that the

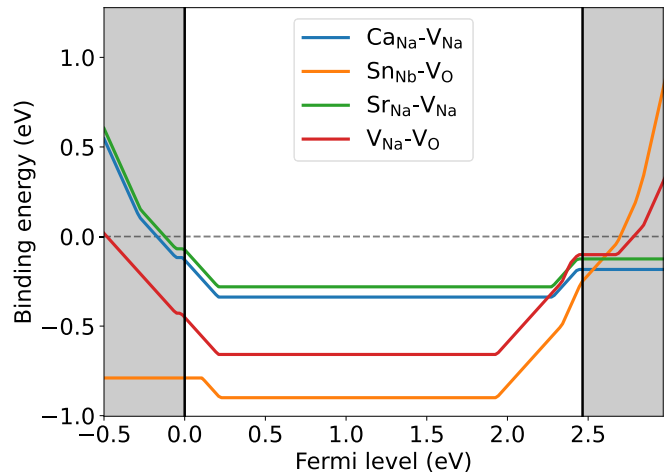

FIG. 8. Binding energy of the defect complexes as a function of the Fermi level. The kinks correspond to charge transition points of the isolated defects.

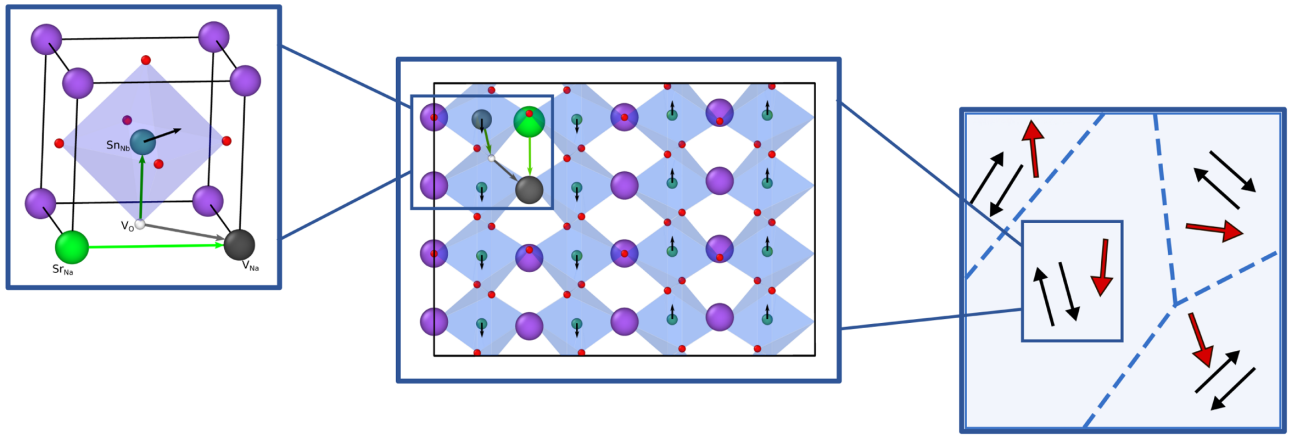

(a) Multiscale representation of defect dipoles, ionic displacement and lattice polarization. The first picture on the left shows pseudo cubic cell. The image in the center shows a 2x2x1 supercell of the orthorhombic cell (space group *Pbcm*) with the antiparallel displacements of Nb atoms. The picture on the right represents schematically the antiferroelectric phase with defect dipoles in different domains.

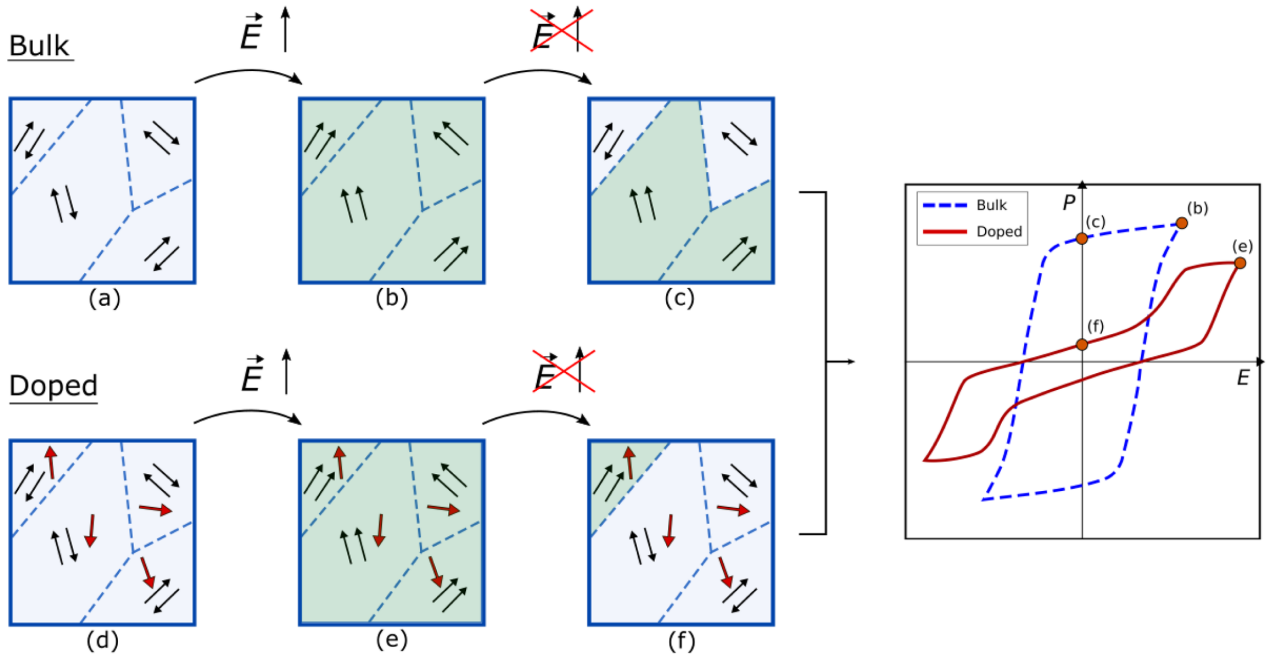

(b) Field switching mechanisms in bulk and doped $NaNbO_3$. In the bulk material, once the electric field is applied, the system undergoes the AFE-FE phase transition (point **b**). When the field is removed, since the FE phase is metastable, not all dipoles can be switched back to an AFE configuration, which results in remanent polirization (point **c**). In the doped case, when the field is removed, the defect dipoles provide an additional restoring force which increases the reversibility of the FE-AFE phase transition (point **f**) and decreases the remanent polarization.

FIG. 9. Schematic representation of the influence of defect dipoles on the *P-E* loops, arising from their interaction with lattice polarization and external field, with consequent contribution in the switching mechanisms.

donor complexes (Sn_{Nb}-V_O and V_{Na}-V_O) become less stable when approaching the CBM. It is interesting to notice that all complexes display a negative binding energy, indicating that single defects gain energy when they associate. This stability indicates that defect dipoles will be present in large concentration. Moreover, introducing a dopant, like $SrSnO_3$, introduces new types of complexes with respect to the bulk phase.

Defect dipoles interact with the lattice polarization in the AFE and FE structures of $NaNbO_3$, as long as with an external electric field. Hence, the presence of defect dipoles is a factor that influences the field switching mechanisms, which ultimately can alter the *P-E* loops, as it has been already suggested both for ferroelectrics and antiferroelectrics [17,50,51]. Figure 9 shows a schematic representation of these concepts. In the bulk material, once the electric field is applied, the system undergoes the AFE-FE phase transition [point *b* in Fig. 9(b)]. When the field is removed, since the FE phase (Q) is metastable, not all dipoles can be switched back to an AFE

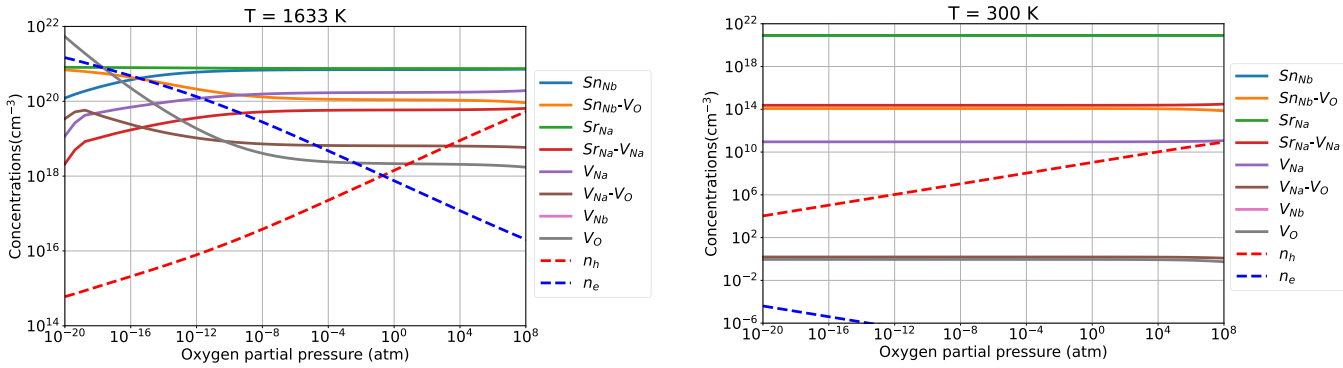

(a) (b)

FIG. 10. Concentrations of defects, electrons (n_e) and holes (n_h) as a function of the oxygen partial pressure.

configuration [9,10], which results in remanent polarization (point c) and a ferroelectric-like P-E loop. Now we look at the doped material. Because in the AFE phase the internal electric field is absent, a distribution of randomly oriented defect dipoles is installed. Moreover, we assume that the kinetics of dipole switching is too slow to be able to follow the electric field, since all the dipoles require multiple diffusion steps to switch direction. In this situation, when the field is removed, the defect dipoles provide an additional restoring force which increases the reversibility of the FE-AFE phase transition (point f). Therefore the remanent polarization is decreased, which consequently increases the recoverable energy.

E. Dependency on oxygen partial pressure

As already mentioned in Sec. II C, experimentally the oxygen chemical potential can be controlled by varying the oxygen partial pressure. Therefore it is useful to calculate the defect concentrations and the electron chemical potential as a function of the partial pressure, in order to be able to relate computational and experimental data. To this day, there is still not reported experimental data of defect concentrations in $NaNbO_3$. We have converted the values of $\Delta\mu_O$ in oxygen partial pressures using Eq. (9), keeping the constraints of the stability over competing phases, which restricts the range of $\Delta\mu_O$. For every oxygen partial pressure, we have solved the charge neutrality condition self-consistently (Sec. II B to find the electron chemical potential). At this point, knowing μ_e, carrier and defect concentrations can be extracted. We have reported the values of the concentrations of holes (n_h), electrons (n_e), and defect concentrations a function of oxygen partial pressure at sintering temperature (1633 K) and room temperature in Fig. 10. Moreover, we have applied the method we have described in Sec. II D to compute μ_e in different quenching conditions, in order to obtain a picture of the possible limit conditions. More specifically, we have considered the equilibrium cases at high and low temperature, the case where all oxygen vacancies are free to equilibrate and Na and Nb vacancies are completely quenched from high to low T, the one where all O vacancies are quenched but the rest are allowed to equilibrate, and finally the one where all intrinsic defects are quenched. As we have already described in Sec. II D, all extrinsic defects are fixed to the experimental concentration of $SrSnO_3$ in sodium niobate. It is important to point out that all of these cases represent extreme situations, almost surely none of those would properly describe reality. However, they are useful because the experimental conditions lie within these limits, which provide a full picture on how quenching of different species influences the defect equilibrium. The results are shown in Fig. 11.

At high temperature and low po_2 [Fig. 10(a)], oxygen vacancies (V_O) and the Sn_{Nb}-V_O complex show the highest concentrations. Both species are donors, resulting in high free electrons concentrations. With increasing po_2, [V_{Na}] increases while the donors concentrations decrease, which results in greater free holes concentrations. The behavior switches from n-type to p-type at po_2 close to 1 atm. At lower temperature [Fig. 10(b)], the dependence of the concentrations on po_2 is less prominent, with [V_{Na}] being the dominant among the charged defects. This results in p-type behavior for all po_2 conditions. For both high and low temperatures the charges of the donor Sr_{Na} and the acceptor Sn_{Nb} compensate each other, having fixed the concentrations of the dopants. The concentrations of defect complexes are large, especially at high temperatures, confirming the expectations given by the negative binding energies (Sec. III D).

The computed electron chemical potentials at which the concentrations in Figs. 10(a) and 10(b) have been determined are shown in Fig. 11 by the blue and orange line, respectively. It is interesting to evaluate how the situation changes

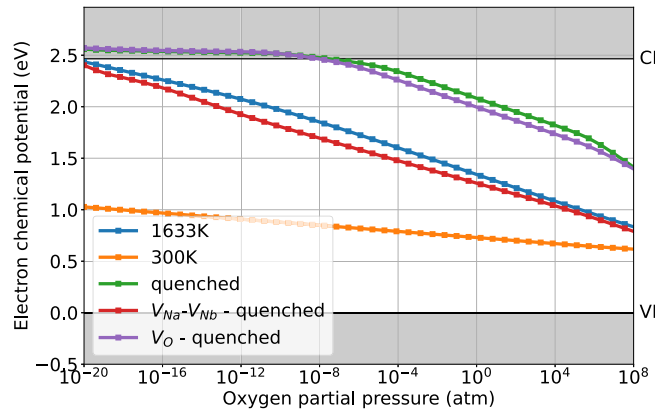

FIG. 11. Electron chemical potential determined self-consistently as a function of the oxygen partial pressure.

TABLE IV. Computed vacancy migration energies in orthorhombic $NaNbO_3$ in units of meV.

Defect	Migration barrier (meV)
$V_{Na,-1}$	1418
$V_{O,+2}$	317

when we introduce quenching conditions. When we quench Na and Nb vacancies, μ_e follows the same trend of the high temperature equilibrium, with a slight shift towards the VBM, as a result of the higher concentration of the acceptor V_{Na} in the low temperature conditions. The equilibrium is modified dramatically if we quench O vacancies. In fact, as it can be seen from Fig. 11, μ_e is shifted upwards towards the CBM, even above CBM for low po_2. This is a result of combined donor contributions which are present in high concentrations in the quenched system, namely V_O, Sn_{Nb}-V_O, and V_{Na}-V_O. The donors dominate even when we quench all defect species, as shown by the green line in Fig. 11. In this case, μ_e still follows the same trend, but it is slightly shifted downwards by the acceptor contribution of V_{Na}.

As stated previously in this section, these conditions represent limit cases and the real situation lies within these limits. In order to determine which of the limit cases is most likely the closest to reality, we have to look at the mobility of the defects. In fact, if a specie is not mobile, it will most likely be quenched when cooling down from synthesis temperature to room temperature. Therefore, we have studied the migration energies of the relevant Na and O vacancies in their most stable charges (-1 and $+2$, respectively) with the method described in Sec. II. The results are shown in Table IV. As expected, the O vacancies are more mobile than Na vacancies. The barrier for V_O is particularly small (only 317 meV), which indicates that it will be considerably mobile and it is unlikely to be completely quenched. V_{Na}, on the other hand, displays a higher barrier (meV), hence a lower mobility and a higher probability to be frozen at room temperature. Therefore we expect that the real case would be closer to the situation where V_{Na} is quenched (shown by the red line in Fig. 11), where quenching leads to the increase in acceptors concentrations and consequently to a shift of the electron chemical potential towards the VBM.

IV. CONCLUSIONS

The formation energies, charge transition levels and doping behavior of intrinsic and extrinsic defects in orthorhombic $NaNbO_3$ doped with Ca,Sr and Sn have been determined by means of density functional theory (DFT). Moreover, four different defect complexes have been studied in different charge states. Lastly, we have developed a method which allows to solve the charge neutrality condition while accounting for defect quenching and fixed dopant concentrations, without neglecting the dependency of their charge state on electron chemical potential and temperature.

We found that Na and O vacancies have low formation energies, while Nb vacancies show much higher formation energies. The formation energies of substitutions with a dopant and defect complexes are in the same range as Na and O vacancies, which explains why it is possible to push the concentrations of dopant up to 5% wt. [8]. All four defect complexes display negative binding energy across all the energy gap, which means that they are stable with respect to the dissociation and they are present in large concentrations, which is confirmed also by the computed oxygen partial pressure dependence of the concentrations in $SrSnO_3$-doped $NaNbO_3$. This suggests that defect complexes have an important contribution in the field switching mechanism, ultimately influencing the AFE *P-E* loops. This calls for a deeper investigation on the nature and kinetics of the switching mechanisms, to reveal how defect dipoles can enhance the reversibility of the AFE-FE phase transition.

Lastly, we have found that quenching can heavily shift the electron chemical potential (Fermi level). When all defect species or just O vacancies are quenched from high to low temperature, the electron chemical potential (μ_e) is pushed close to the conduction band minimum. The opposite happens if we quench Nb and Na vacancies, with μ_e being shifted slightly towards the valence band maximum. The computed migration barriers, 317 meV for V_O and 1418 meV for V_{Na}, suggest that O vacancies are much more mobile, therefore the scenario where only Na vacancies are quenched is likely closer to the situation at the synthesis stage. This shows how the electron chemical potential can be engineered not just by doping, but also by tailoring the synthesis conditions.

ACKNOWLEDGMENTS

This work was supported by the Hessian State Ministry for Higher Education, Research and the Arts under the LOEWE collaborative project "FLAME." Financial support by the Deutsche Forschungsgemeinschaft under Contract No. AL-578/23-1 is also gratefully acknowledged. The authors gratefully acknowledge the computing time granted by the NHR4CES Resource Allocation Board and provided on the supercomputer Lichtenberg II at TU Darmstadt as part of the NHR4CES infrastructure. The calculations for this research were conducted with computing resources under the Project No. 1596.

There are no conflicts of interest to declare.

[1] Z. Liu, T. Lu, J. Ye, G. Wang, X. Dong, R. Withers, and Y. Liu, Adv. Mater. Technol. **3**, 1800111 (2018).
[2] D. Fritsch, Adv. Mater. Sci. Eng., 6416057 (2018).
[3] L. Yang, X. Kong, F. Li, H. Hao, Z. Cheng, H. Liu, J.-F. Li, and S. Zhang, Adv. Mater. Sci. Eng **102**, 72 (2019).
[4] H. D. Megaw, Ferroelectrics **7**, 87 (1974).
[5] A. Kania and J. Kwapulinski, J. Phys.: Condens. Matter **11**, 8933 (1999).
[6] J. Koruza, J. Tellier, B. Malič, V. Bobnar, and M. Kosec, J. Appl. Phys. **108**, 113509 (2010).
[7] R. Machado, M. Sepliarsky, and M. G. Stachiotti, Phys. Rev. B **84**, 134107 (2011).

[8] M.-H. Zhang, N. Hadaeghi, S. Egert, H. Ding, H. Zhang, P. B. Groszewicz, G. Buntkowsky, A. Klein, and J. Koruza, Chem. Mater. **33**, 266 (2021).
[9] H. Guo, H. Shimizu, Y. Mizuno, and C. A. Randall, J. Appl. Phys. **118**, 054102 (2015).
[10] S. Egert, M.-H. Zhang, J. Koruza, P. B. Groszewicz, and G. Buntkowsky, J. Phys. Chem. C **124**, 23852 (2020), publisher: American Chemical Society.
[11] Y. Feng, J. Wu, Q. Chi, W. Li, Y. Yu, and W. Fei, Chem. Rev. **120**, 1710 (2020).
[12] L. Gao, H. Guo, S. Zhang, and C. A. Randall, Appl. Phys. Lett. **112**, 092905 (2018).
[13] H. Guo, H. Shimizu, Y. Mizuno, and C. A. Randall, J. Appl. Phys. **117**, 214103 (2015).
[14] L. Gao, H. Guo, S. Zhang, and C. A. Randall, J. Appl. Phys. **120**, 204102 (2016).
[15] H. Shimizu, H. Guo, S. E. Reyes-Lillo, Y. Mizuno, K. M. Rabe, and C. A. Randall, Dalton Transactions **44**, 10763 (2015).
[16] J. Ye, G. Wang, X. Chen, F. Cao, and X. Dong, Appl. Phys. Lett. **114**, 122901 (2019).
[17] J. Hao, Z. Xu, R. Chu, W. Li, J. Du, P. Fu, and G. Li, J. Am. Ceram. Soc. **99**, 402 (2016).
[18] M. Jiang, X. Li, J. Zhu, X. Zhu, W. Shi, L. Li, D. Xiao, and J. Zhu, Curr. Appl. Phys. **10**, 526 (2010).
[19] X. Tan, Z. Xu, X. Liu, and Z. Fan, Mater. Res. Lett. **6**, 159 (2018).
[20] A. Shigemi and T. Wada, Jpn. J. Appl. Phys. **43**, 6793 (2004).
[21] L. Villa, E. Ghorbani, and K. Albe, J. Appl. Phys. **131**, 124106 (2022).
[22] S. Shousha, S. Khalil, and M. Youssef, Phys. Chem. Chem. Phys. **22**, 6308 (2020).
[23] J. Lee and S. Han, Phys. Chem. Chem. Phys. **15**, 18906 (2013).
[24] G. Kresse and J. Hafner, Phys. Rev. B **47**, 558 (1993).
[25] G. Kresse and J. Hafner, Phys. Rev. B **49**, 14251 (1994).
[26] G. Kresse and J. Furthmüller, Comput. Mater. Sci. **6**, 15 (1996).
[27] G. Kresse and J. Furthmüller, Phys. Rev. B **54**, 11169 (1996).
[28] P. E. Blöchl, Phys. Rev. B **50**, 17953 (1994).
[29] G. Kresse and D. Joubert, Phys. Rev. B **59**, 1758 (1999).
[30] J. P. Perdew, K. Burke, and M. Ernzerhof, Phys. Rev. Lett. **77**, 3865 (1996).
[31] F. Birch, Phys. Rev. **71**, 809 (1947).
[32] F. D. Murnaghan, Proc. Natl. Acad. Sci. USA **30**, 244 (1944).
[33] G. Henkelman, G. Jóhannesson, and H. Jónsson, in *Theoretical Methods in Condensed Phase Chemistry*, edited by S. D. Schwartz (Kluwer Academic Publishers, Dordrecht, 2002), Vol. 5, pp. 269–302, Progress in Theoretical Chemistry and Physics
[34] G. Henkelman, B. P. Uberuaga, and H. Jónsson, J. Chem. Phys. **113**, 9901 (2000).
[35] G.-X. Qian, R. M. Martin, and D. J. Chadi, Phys. Rev. B **38**, 7649 (1988).
[36] S. B. Zhang, S.-H. Wei, and A. Zunger, J. Appl. Phys. **83**, 3192 (1998).
[37] Y.-J. Zhao, C. Persson, S. Lany, and A. Zunger, Appl. Phys. Lett. **85**, 5860 (2004).
[38] Y. Kumagai and F. Oba, Phys. Rev. B **89**, 195205 (2014).
[39] A. Jain, J. Montoya, S. Dwaraknath, N. E. R. Zimmermann, J. Dagdelen, M. Horton, P. Huck, D. Winston, S. Cholia, S. P. Ong, and K. Persson, in *Handbook of Materials Modeling*, edited by W. Andreoni and S. Yip (Springer International Publishing, Cham, 2018), pp. 1–34.
[40] S. P. Ong, S. Cholia, A. Jain, M. Brafman, D. Gunter, G. Ceder, and K. A. Persson, Comput. Mater. Sci. **97**, 209 (2015).
[41] S. P. Ong, W. D. Richards, A. Jain, G. Hautier, M. Kocher, S. Cholia, D. Gunter, V. L. Chevrier, K. A. Persson, and G. Ceder, Comput. Mater. Sci. **68**, 314 (2013).
[42] S. P. Ong, L. Wang, B. Kang, and G. Ceder, Chem. Mater. **20**, 1798 (2008).
[43] K. Reuter and M. Scheffler, Phys. Rev. B **65**, 035406 (2001).
[44] P. Erhart and K. Albe, J. Appl. Phys. **104**, 044315 (2008).
[45] D. R. Stull and H. Prophet, *JANAF Thermochemical Tables*, 2nd ed. (1971).
[46] P. Canepa, G. Sai Gautam, D. Broberg, S.-H. Bo, and G. Ceder, Chem. Mater. **29**, 9657 (2017).
[47] P. Li, S. Ouyang, G. Xi, T. Kako, and J. Ye, J. Phys. Chem. C **116**, 7621 (2012).
[48] A. Jain, S. P. Ong, G. Hautier, W. Chen, W. D. Richards, S. Dacek, S. Cholia, D. Gunter, D. Skinner, G. Ceder, and K. A. Persson, APL Mater. **1**, 011002 (2013).
[49] M.-H. Zhang, C. Zhao, L. Fulanović, J. Rödel, N. Novak, A. Schökel, and J. Koruza, Appl. Phys. Lett. **118**, 132903 (2021).
[50] L. Jiang, D. C. Mitchell, W. Dmowski, and T. Egami, Phys. Rev. B **88**, 014105 (2013).
[51] X. Ren, Nat. Mater. **3**, 91 (2004).